

Memristors-coupled neuron models with multiple firing patterns and homogeneous and heterogeneous multistability

Xuan Wang(王暄), Santo Banerjee, Yinghong Cao(曹颖鸿), and Jun Mou(牟俊)

Citation: Chin. Phys. B, 2024, 33 (**10**): 100501. DOI: 10.1088/1674-1056/ad6256
Journal homepage: http://cpb.iphy.ac.cn; http://iopscience.iop.org/cpb

What follows is a list of articles you may be interested in

Dynamics and synchronization of neural models with memristive membranes under energy coupling

Jingyue Wan(万婧玥), Fuqiang Wu(吴富强), Jun Ma(马军), and Wenshuai Wang(汪文帅)
Chin. Phys. B, 2024, 33 (**5**): 050504. DOI: 10.1088/1674-1056/ad1dcc

Fractional-order heterogeneous memristive Rulkov neuronal network and its medical image watermarking application

Dawei Ding(丁大为), Yan Niu(牛炎), Hongwei Zhang(张红伟), Zongli Yang(杨宗立), Jin Wang(王金), Wei Wang(王威), and Mouyuan Wang(王谋媛)
Chin. Phys. B, 2024, 33 (**5**): 050503. DOI: 10.1088/1674-1056/ad322b

Dynamics analysis and cryptographic implementation of a fractional-order memristive cellular neural network model

Xinwei Zhou(周新卫), Donghua Jiang(蒋东华), Jean De Dieu Nkapkop, Musheer Ahmad, Jules Tagne Fossi, Nestor Tsafack, and Jianhua Wu(吴建华)
Chin. Phys. B, 2024, 33 (**4**): 040506. DOI: 10.1088/1674-1056/ad03dd

Coexistence behavior of asymmetric attractors in hyperbolic-type memristive Hopfield neural network and its application in image encryption

Xiaoxia Li(李晓霞), Qianqian He(何倩倩), Tianyi Yu(余天意),Zhuang Cai(才壮), and Guizhi Xu(徐桂芝)
Chin. Phys. B, 2024, 33 (**3**): 030505. DOI: 10.1088/1674-1056/acf281

Multiple mixed state variable incremental integration for reconstructing extreme multistability in a novel memristive hyperchaotic jerk system with multiple cubic nonlinearity

Meng-Jiao Wang(王梦蛟) and Lingfang Gu(辜玲芳)
Chin. Phys. B, 2024, 33 (**2**): 020504. DOI: 10.1088/1674-1056/acddd0

Memristors-coupled neuron models with multiple firing patterns and homogeneous and heterogeneous multistability

Xuan Wang(王暄)[1], Santo Banerjee[2], Yinghong Cao(曹颖鸿)[1], and Jun Mou(牟俊)[1,†]

[1] *School of Information Science and Engineering, Dalian Polytechnic University, Dalian* 116034, *China*
[2] *Department of Mathematical Sciences, Giuseppe Luigi Lagrange, Politecnico di Torino, Corso Duca degli Abruzzi* 24, *Torino, Italy*

(Received 19 June 2024; revised manuscript received 8 July 2024; accepted manuscript online 12 July 2024)

Memristors are extensively used to estimate the external electromagnetic stimulation and synapses for neurons. In this paper, two distinct scenarios, i.e., an ideal memristor serves as external electromagnetic stimulation and a locally active memristor serves as a synapse, are formulated to investigate the impact of a memristor on a two-dimensional Hindmarsh–Rose neuron model. Numerical simulations show that the neuronal models in different scenarios have multiple burst firing patterns. The introduction of the memristor makes the neuronal model exhibit complex dynamical behaviors. Finally, the simulation circuit and DSP hardware implementation results validate the physical mechanism, as well as the reliability of the biological neuron model.

Keywords: memristor, multistability, Hamilton energy, firing pattern, Neuron model, hardware implementation

PACS: 05.45.–a, 05.45.Gg **DOI:** 10.1088/1674-1056/ad6256

1. Introduction

The human brain's neural system consists of a large number of neurons, which are interconnected to form a complex and precise network system.[1] Neurophysiological studies have shown that electrical activity between neurons usually exhibits enriched nonlinear dynamical behavior.[2] Exploring the dynamical properties of biological neurons is of key significance for understanding the activities of the biological nervous system.[3–5] Scholars have successively proposed various artificial neuron models, including the Hodgkin–Huxley neuron model,[6] the Hindmarsh–Rose (HR) neuron model,[7] the FitzHugh–Nagumo neuron model,[8,9] and the Izhikevich neuron model.[10] Among these, the HR neuron model has received widespread attention because of its simple structure and its ability to flexibly simulate different behaviors and complex electrical activities of biological neurons.[11–14]

In fact, neuronal membranes have specialized ion channels that allow ions such as calcium, potassium, and chloride to pass through the neuronal membrane. When these ions cross the neuronal membrane, it alters the concentration of ions inside and outside the membrane, which triggers the electromagnetic induction effect to generate action potentials. In biological neuron models, the question of how to more accurately respond to this electrical activity relationship has become a research hotspot.[15–19] Currently, researchers are focusing on utilizing an emerging component,[20] the magnetic-controlled memristor, to describe the dynamical relationship between magnetic flux and membrane potential.[21–23] The introduction of the memristor into neuronal models has revealed a rich array of firing activities.[24] Memristor neuron models exhibit different firing patterns such as spiking, bursting and chaos as system parameters and external stimuli are changed.[25–27] This makes it possible to understand the excitation of biological neurons and to modulate them.

Local activity is considered to be the origin of complexity.[28] A memristor with locally active properties is called a locally active memristor (LAM). A concept is expanded from continuous to discrete,[29,30] and researchers have proposed a number of models and used them for circuit design[31–33] and system construction.[34–41] Compared to an ideal memristor, a LAM is able to amplify small energy fluctuations, thus reducing energy loss. This ability can play an important role in biological neuron simulation.[42] LAMs have contributed to the development of neurodynamics. Researchers are increasingly concerned that the use of LAMs to simulate biological synapses is becoming a trend in biological neuron research. Lai *et al.* used the memristor to construct a discrete neural network model and demonstrated that the introduction of the memristor can induce complex dynamical behaviors in the neural network.[43] Ma *et al.* applied the LAM to a model of an HR neuron and rotationally controlled the firing generated by it.[44] Li *et al*. designed a LAM with memristive parameters capable of influencing local activity and used it as a connecting synapse, and found rich firing behavior.[45]

The behavioral mechanisms between neurons in the brain are very complex, and the multistable behavior is decisive for the information storage and processing of biological neurons.[46] That is, for biological neuron models, the number of attractors corresponds to the strength of the brain's memory capacity. Revealing the complex multistability of neuron

†Corresponding author. E-mail: moujun@dlpu.edu.cn

© 2024 Chinese Physical Society and IOP Publishing Ltd

models has increasingly become a focus of attention.[47–50] Hu *et al*. reported an improved HR neuronal model, discovered a bubble-like bifurcation pattern, and analyzed the heterogeneous multistability.[51] Santana *et al*. found the presence of multistability of FHN neurons under two electrical interactions.[52] Nevertheless, studies on homogeneous extreme multistability in neuron models are relatively scarce.

Inspired by the above, this paper introduces an ideal memristor and a LAM into the two-dimensional (2D) HR neuron model, respectively, and establishes two scenarios describing external electromagnetic stimulation and synaptic simulation. Bifurcation analysis and other means are used to explore how neurons respond to various excitations. Meanwhile, the neuron models under different scenarios are able to generate rich electrical activities. Interestingly, homogeneous extreme multistability and heterogeneous multistability were found in the two scenarios, respectively. The results show that introducing memristors suitable for different scenarios into the neuronal model can enable the neurons to generate complex dynamical behaviors and significantly increase the complexity of the model. Finally, both the simulated circuit and the developed DSP hardware implementation proved the physical realizability of the designed models.

The rest of this paper is organized as follows. In Section 2, the ideal memristor model is introduced and a new LAM based on the ideal memristor is proposed. In Section 3, the neuron models under different scenarios are constructed and the equilibrium points are analyzed. A series of complex dynamical behaviors of the neuron models in different scenarios are explored in Section 4. Section 5 utilizes analog circuits and develops a digital platform to hardware implement the neuron models in different scenarios. Conclusions are given in Section 6.

2. Memristor modeling

In this section, an ideal memristor with trigonometric functions is presented, and based on this a novel locally active and nonvolatile memristor is proposed.

2.1. Ideal memristor

An ideal memristor containing sine memristance states with a classical structure can be expressed as

$$\begin{cases} i_{\mathrm{M}} = (a^2 + b\sin(\varphi))v_{\mathrm{M}}, \\ \dot{\varphi} = v_{\mathrm{M}}, \end{cases} \tag{1}$$

where i_{M} and v_{M} are the outputs and inputs of an ideal memristor, φ is the internal state variable of the memristor, and a and b are the parameters of the memristor. A sinusoidal voltage of $V = A\sin(2\pi ft)$ is given as input, and the fingerprint of the ideal memristor is studied by adjusting different frequencies and amplitudes. Keeping the amplitude as 5 V and the frequency selected as 3 Hz, 10 Hz, and 50 Hz, the pinch hysteresis loops are shown in Fig. 1(a).

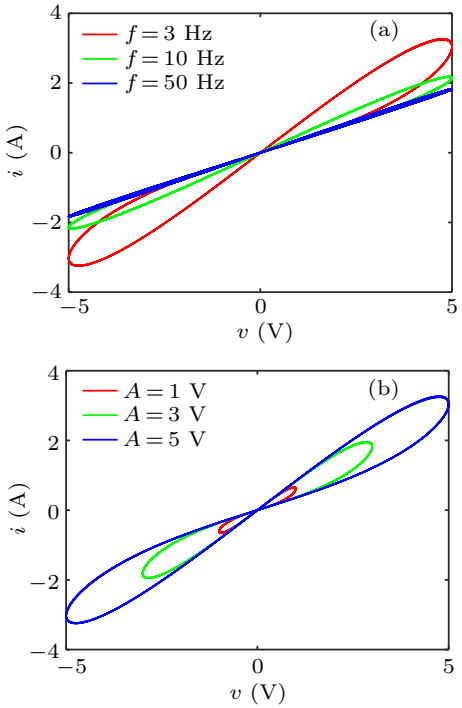


Fig. 1. Pinch hysteresis loops of the ideal memristor. (a) $A = 5$ V, different frequencies; (b) $f = 3$ Hz, different amplitudes.

It can be seen that with the increase of the frequency for the memristor, the pinch hysteresis loops of the side flap area gradually decrease and when the frequency reaches 50 Hz, the memristor is close to the degradation of a linear resistor and the pinch hysteresis loops approximate to become a linear function in the figure. When the frequency is 3 Hz and the amplitude is selected as 1 V, 3 V, and 5 V, the shape of the pinch hysteresis loops of the memristor is unchanged, and the area of the side flap expands with the increase of the amplitude, as shown in Fig. 1(b).

2.2. Locally active memristor

Based on the ideal memristor, by revising the equation of state, a completely new LAM is obtained, which is denoted as

$$\begin{cases} i_{\mathrm{M}} = G(x)v_{\mathrm{M}}, \\ G(x) = a^2 + b\sin(x), \\ \dot{x} = 2\tanh(x) - x - v_{\mathrm{M}}. \end{cases} \tag{2}$$

The parameters a and b for the novel LAM are 0.2 and -1, respectively, and a sinusoidal voltage of the same adjustable frequency and amplitude is applied across its terminals to obtain the pinch hysteresis loops of the memristor, as shown in Fig. 2.

It is evident that pinch hysteresis loops consistent with the characteristics of the memristor are exhibited at different frequencies and amplitudes. Interestingly, coexisting pinch hysteresis loops appear under the initial conditions of the memristor with $x(0) = \pm 3$, respectively, which indicates the bistable

behavior of the newly designed LAM. The time-domain waveforms for both current and voltage show that besides the point where both voltage and current are zero at the same time, indicated by black dots, there is also a point where the current is zero but the voltage is not zero, indicated by green dots, which is a unique property of the LAM.

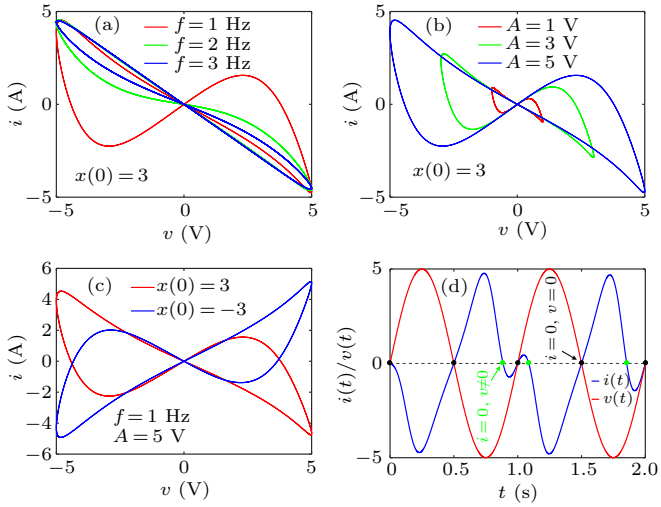


Fig. 2. Pinch hysteresis loops and time-domain waveforms: (a) different frequencies when $A=5$ V; (b) different amplitudes when $f=1$ Hz; (c) different initial conditions when $A=5$ V, $f=1$ Hz; (d) time-domain waveforms.

If the power of the LAM is turned off, the memristor is in the de-energized state, i.e., $v_{\rm M}=0$. The equation of state of the memristor at this time is expressed as

$$\dot{x}|_{v_{\rm M}=0} = 2\tanh(x) - x. \tag{3}$$

Its power-off plot (POP) is a continuous single-valued function curve, as shown in Fig. 3(a). The LAM has two stable equilibrium points and one unstable equilibrium point, which proves that the memristor is nonvolatile. The locally active characteristics of the memristor can be visually verified from the DC V–I plot. Using the DC voltage V and $x=0$ to drive the memristor, the functions of DC voltage V and DC current I can be obtained by Eq. (2), and they are plotted in the V–I plane as shown in Fig. 3(b). The green curved portion of the figure corresponds to the locally active region of the memristor. All locally active and locally passive regions of the memristor are listed in Table 1.

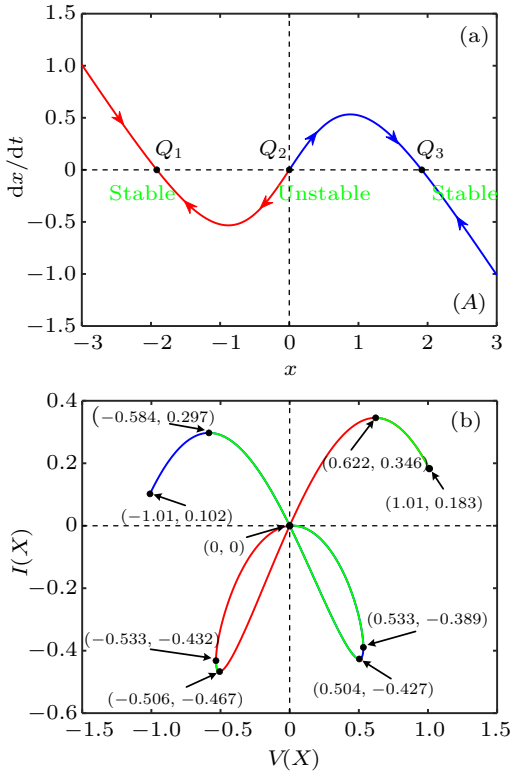


Fig. 3. Nonvolatile and locally active properties of the LAM: (a) POP; (b) DC V–I plot.

Table 1. Analysis of locally active and locally passive regions.

Range of the state variable X	Slope of the DC V–I plot	Characteristics of the memristor	Range of the voltage V (V)	Range of the current I (A)
[–3, –2.599]	negative slope	locally active	[0.622, 1.010]	[0.183, 0.346]
(–2.599, –1.082]	positive slope	locally passive	[–0.506, 0.622)	[–0.467, 0.346)
(–1.082, –0.882]	negative slope	locally active	(–0.533, –0.506)	(–0.467, –0.432)
(–0.882, 0]	positive slope	locally passive	[–0.533, 0]	[–0.432, 0]
(0, 0.882]	negative slope	locally active	(0, 0.533)	(–0.389, 0)
(0.882, 1.092]	positive slope	locally passive	[0.504, 0.533]	[–0.427, –0.389]
(1.092, 2.559]	negative slope	locally active	(–0.584, 0.504)	(–0.427, 0.297)
(2.559, 3]	positive slope	locally passive	[–1.01, –0.584]	[0.102, 0.297]

3. Memristor-HR neuron modeling

The LAM is an ideal component for simulating neural synapses. In this paper, an ideal memristor and a LAM are used to simulate external electromagnetic stimulation and synapses of neurons, respectively. Novel neuron models are investigated under two scenarios of introducing external electromagnetic stimulation and simulating synapses.

3.1. Scene modeling

The classical 2D HR neuron model can be mathematically represented as

$$\begin{cases} \dot{x} = y - \alpha x^3 + \beta x^2 + I, \\ \dot{y} = \gamma - \theta x^2 - y, \end{cases} \tag{4}$$

where x indicates the membrane potential and the spiking variable of a neuron is denoted by y. α, β, γ, and θ are parameters associated with the neuron model, and I denotes the external current, which is usually positive.

Scenario I: Ideal memristor serves as external electromagnetic stimulation.

Under the ideal memristor as external stimulus condition, the ideal memristor model is introduced into the HR neuron model, and defined as

$$\begin{cases} \dot{x}_{\mathrm{EMR}} = y_{\mathrm{EMR}} - 1.2{x_{\mathrm{EMR}}}^3 + 3{x_{\mathrm{EMR}}}^2 \\ \qquad + k_1(a_1^2 + b_1\sin(\varphi))x_{\mathrm{EMR}} + I_1, \\ \dot{y}_{\mathrm{EMR}} = 1 - 5{x_{\mathrm{EMR}}}^2 - y_{\mathrm{EMR}}, \\ \dot{\varphi} = x_{\mathrm{EMR}}, \end{cases} \tag{5}$$

where φ denotes the magnetic flux of the membrane potential x. $k_1(a_1 + b_1\sin(\varphi))x_{\mathrm{EMR}}$ denotes the external electromagnetic stimulus, and k_1 denotes the external electromagnetic stimulus intensity. a_1 and b_1 are the ideal memristor control parameters and the parameters of the HR neuron model were determined as $\alpha = 1.2$, $\beta = 3$, $\gamma = 1$, and $\theta = 5$.

Scenario II: The LAM serves as synapse of the neuronal model.

The proposed LAM is introduced into the HR neural model as neural synapse, which is denoted as

$$\begin{cases} \dot{x}_{\mathrm{SYP}} = y_{\mathrm{SYP}} - 1.2{x_{\mathrm{SYP}}}^3 + 3{x_{\mathrm{SYP}}}^2 \\ \qquad + k_2(a_2^2 + b_2\sin(z_{\mathrm{SYP}}))x_{\mathrm{SYP}} + I_2, \\ \dot{y}_{\mathrm{SYP}} = 1 - 5{x_{\mathrm{SYP}}}^2 - y_{\mathrm{SYP}}, \\ \dot{z}_{\mathrm{SYP}} = 2\tanh(z_{\mathrm{SYP}}) - z_{\mathrm{SYP}} - x_{\mathrm{SYP}}, \end{cases} \tag{6}$$

where k_2 is the synaptic coupling strength, while a_2 and b_2 are the control parameters of the LAM. The model structure diagrams for the two scenarios are shown in Fig. 4.

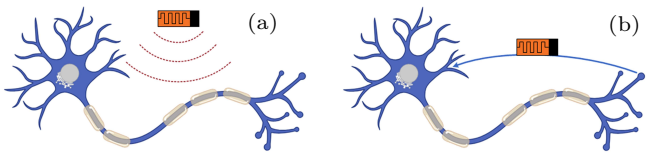


Fig. 4. Schematic of the scenarios: (a) neuronal structures with electromagnetic radiation; (b) neuronal structures with a memristive synapse.

3.2. Equilibrium point analysis

Numerical and graphical methods were used to analyze the equilibrium points of the neuron model and its stability in different scenarios. For scenario I, making the right-hand of the differential equation equal to zero gets

$$\begin{cases} y_{\mathrm{EMR}} - 1.2{x_{\mathrm{EMR}}}^3 + 3{x_{\mathrm{EMR}}}^2 + k_1({a_1}^2 \\ \quad + b_1\sin(\varphi))x_{\mathrm{EMR}} + I_1 = 0, \\ 1 - 5{x_{\mathrm{EMR}}}^2 - y_{\mathrm{EMR}} = 0, \\ x_{\mathrm{EMR}} = 0. \end{cases} \tag{7}$$

The third equation of Eq. (7) is brought into the first and second equations and found to be contradictory, so there is no equilibrium point in the neuron model for this scenario. Setting the parameters $a_1 = 0.5$, $b_1 = 1$, $k_1 = 1$, $I_1 = 0.6$ and the initial conditions as $(0, 0, \pi)$, its three Lyapunov exponents are $(\mathrm{LE}_1, \mathrm{LE}_2, \mathrm{LE}_3) = (0.1, 0, -3.5)$. This means that the neuron model in this scenario is a chaotic system with hidden attractors, and its generated hidden chaotic attractors are illustrated in Fig. 5.

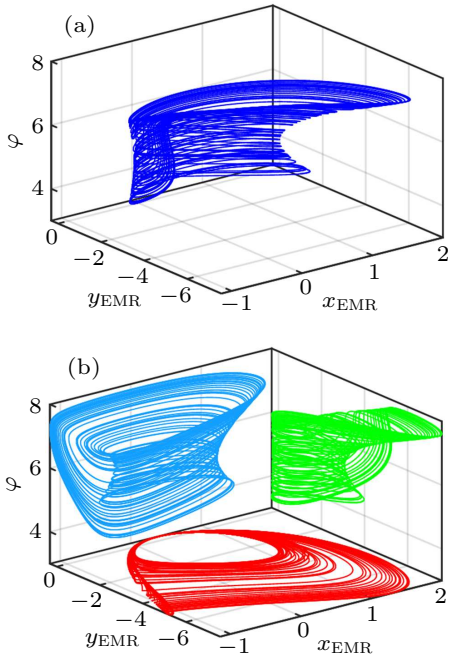


Fig. 5. The chaotic attractor in scenario I: (a) 3D phase space; (b) 2D planar projection.

For scenario II, the same can be obtained

$$\begin{cases} y_{\mathrm{SYP}} - 1.2{x_{\mathrm{SYP}}}^3 + 3{x_{\mathrm{SYP}}}^2 + k_2({a_2}^2 \\ \quad + b_2\sin(z_{\mathrm{SYP}}))x_{\mathrm{SYP}} + I_2 = 0, \\ 1 - 5{x_{\mathrm{SYP}}}^2 - y_{\mathrm{SYP}} = 0, \\ 2\tanh(z_{\mathrm{SYP}}) - z_{\mathrm{SYP}} - x_{\mathrm{SYP}} = 0. \end{cases} \tag{8}$$

To find the equilibrium point for scenario II, the second and third equations in Eq. (8) are used to express the first equation as a one-variable function F containing only the variable z_{SYP}, denoted

$$\begin{aligned} F(z_{\mathrm{SYP}}) \;=\; & 1 - 5(2\tanh(z_{\mathrm{SYP}}) - z_{\mathrm{SYP}})^2 \\ & - 1.2(2\tanh(z_{\mathrm{SYP}}) - z_{\mathrm{SYP}})^3 \\ & + 3(2\tanh(z_{\mathrm{SYP}}) - z_{\mathrm{SYP}})^2 \\ & + k_2({a_2}^2 + b_2\sin(z_{\mathrm{SYP}})) \\ & \times (2\tanh(z_{\mathrm{SYP}}) - z_{\mathrm{SYP}}) + I_2. \end{aligned} \tag{9}$$

The function curve of this function is plotted as shown in Fig. 6(a). The final equilibrium point of the model for this scenario is obtained as (0.936, −3.384, −2.925). The Jacobi matrix of the system is found to be

$$J=\begin{vmatrix} 6x_{\rm SYP}+k_2(a_2{}^2+b_2\sin(z_{\rm SYP}))-3.6x_{\rm SYP}{}^2 & 1 & b_2k_2x_{\rm SYP}\cos(z_{\rm SYP}) \\ -10x_{\rm SYP} & -1 & 0 \\ -1 & 0 & 1-2\tanh^2(z_{\rm SYP}) \end{vmatrix}. \tag{10}$$

The parameters of the neuron model in this scenario are set to $a_2=0.2$, $b_2=1$, $k_2=1$, and $I_2=1.5$, and the equilibrium points are brought into the Jacobi matrix to obtain the characteristic equation as

$$|\lambda E-J|=\lambda^3-0.397\lambda^2+4.906\lambda+6. \tag{11}$$

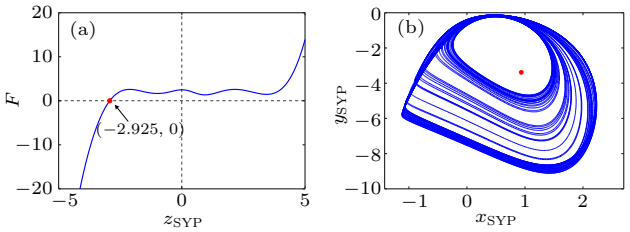


Fig. 6. Solve function curve at equilibrium point; (b) chaotic attractor phase trajectory.

The eigenvalues of the model are obtained as $\lambda_{1,2}=0.642\pm2.397$i and $\lambda_3=-0.975$. The eigenvalues λ_1 and λ_2 are a pair of conjugate complex roots with a positive real part, while the eigenvalue λ_3 is a positive real number, so that this equilibrium point corresponds to the saddle-focus point of the indicator-2. In general, the saddle-focus equilibrium point of indicator-2 is the key to generating chaotic behavior, and it is also a prerequisite for vortex generation. This also confirms the existence of chaotic properties of the neuron model in this scenario. The phase diagram of the chaotic attractor generated by the neuronal model is shown in Fig. 6(b), where the chaotic attractor equilibrium point is indicated by a red dot in the figure.

4. Dynamical analysis

4.1. Basic dynamical analysis

For different scenarios, the bifurcation diagrams and Lyapunov exponential spectrum of the memristor parameter a, strength parameter k, and the externally forced current I in their adjustable intervals are examined, with the initial conditions fixed to $(0, 0, \pi)$.

Scenario I: The parameters in the model are specified as $b_1=1$, the parameter a_1 of the memristor varies in the range of [0, 0.8], the electromagnetic induction strength k_1 increases at [0.5, 1], and the bifurcation diagrams and the Lyapunov exponential spectra of the external forcing currents I_1 varying in [0, 2] are plotted in Fig. 7. When the parameter a_1 of the memristor and the electromagnetic induction strength k_1 are varied, the neuron system into the chaotic status by means of the period doubling-bifurcation, whereas for parameter I_1, the neuron system enters the paroxysmal chaotic state due to the presence of the tangential bifurcation, and then it enters the periodic state by the inverse period-doubling bifurcation.

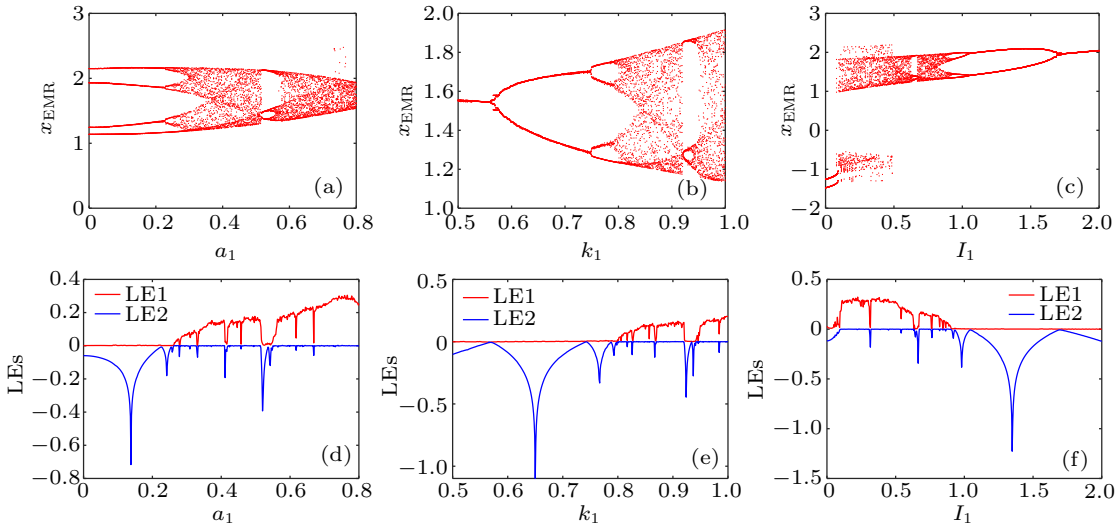


Fig. 7. The bifurcation diagrams and Lyapunov exponent spectra for typical parameters of the system in scenario I: (a), (d) the ideal memristor's parameter a_1; (b), (e) electromagnetic induction strength parameter k_1 of the ideal memristor; (c), (f) forced current I_1.

Without loss of generality, a representative parameter was chosen for the electromagnetic induction strength k_1, which partially shows the neuron model's firing pattern in this scenario, as shown in Fig. 8. The left-hand side of Fig. 8 shows the timing diagram of the external electromagnetic stimulus φ, and the right-hand side shows the corresponding phase diagram in the φ–y plane. The model exhibits period-1 spiking, period-2 spiking, period-4 spiking and chaotic spiking firing patterns at electromagnetic induction strengths $k_1=0.53$, 0.65, 0.77, and 0.85, respectively.

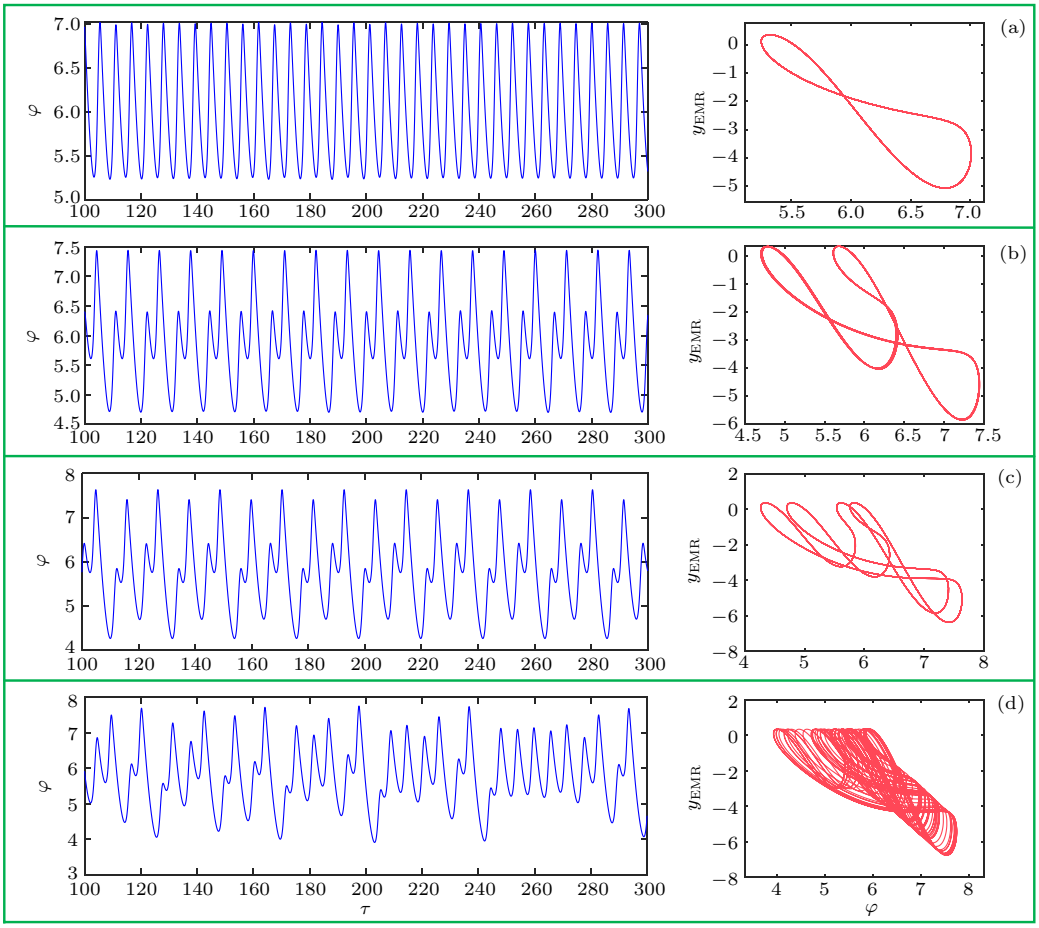


Fig. 8. Different firing patterns exhibited under various parameters of electromagnetic induction strengths: (a) $k_1 = 0.53$, period-1 spiking; (b) $k_1 = 0.65$, period-2 spiking; (c) $k_1 = 0.77$, period-4 spiking; (d) $k_1 = 0.85$, chaotic spiking.

The neuronal membrane potential energy consumption and energy supply determine the shift in the firing pattern. According to Helmholtz's theorem, the neuron model equation can be expressed in vector field form, written as

$$\dot{V} = f_{\rm c}(V) + f_{\rm d}(V) + h(V)z(V,t), \tag{12}$$

where $f_{\rm c}(V)$ denotes the divergence-free vector about the energy storage, $f_{\rm d}(V)$ denotes the gradient vector of the sum of the generated energy and the consumed energy, and $h(V)z(V,t)$ is the external energy supply. Therefore, the dynamical equations of scenario I can be expressed through Eq. (12) as

$$\begin{bmatrix} \dot{x}_{\rm EMR} \\ \dot{y}_{\rm EMR} \\ \dot{\varphi} \end{bmatrix} = \begin{bmatrix} I_1 \\ 0 \\ 0 \end{bmatrix} + \begin{bmatrix} y_{\rm EMR} - k_1(a_1^2 + b_1\varphi) \\ 1 - 5x_{\rm EMR}^2 \\ x_{\rm EMR} \end{bmatrix} + \begin{bmatrix} -1.2{x_{\rm EMR}}^3 + 3{x_{\rm EMR}}^2 + k_1(a_1^2 + b_1\sin\varphi)x_{\rm EMR} + k(a_1^2 + b_1\varphi) \\ -y_{\rm EMR} \\ 0 \end{bmatrix}. \tag{13}$$

The derivative of the energy function $H(V)$ along the direction of the conservation field should be zero, so the Hamiltonian energy can be defined as

$$\begin{aligned} &\nabla H^{\rm T}(V) f_{\rm c}(V) \\ &= (y_{\rm EMR} - k_1({a_1}^2 + b_1\varphi))\frac{\partial H}{\partial x_{\rm EMR}} \\ &\quad + (1 - 5{x_{\rm EMR}}^2)\frac{\partial H}{\partial y_{\rm EMR}} + x\frac{\partial H}{\partial \varphi} = 0. \end{aligned} \tag{14}$$

The final Hamiltonian energy function is obtained as

$$H = \frac{2}{3}5{x_{\rm EMR}}^3 - 2x_{\rm EMR} + (y_{\rm EMR} - b_1\varphi)^2 + b_1{x_{\rm EMR}}^2. \tag{15}$$

The rate of change of the Hamiltonian energy can be obtained through Eq. (15), which can be expressed by substituting the differential equation of the system as

$$\begin{aligned} \dot{H} &= 2(5x_{\rm EMR}^2 - 1 + b_1 x_{\rm EMR}^2)\dot{x} \\ &\quad + 2(y_{\rm EMR} - b_1\varphi)\dot{y}_{\rm EMR} - 2b_1(y_{\rm EMR} - b_1\varphi)\dot{\varphi} \end{aligned}$$

$$
\begin{aligned}
= {} & (10-2x_{\mathrm{EMR}}^2+2b_1x_{\mathrm{EMR}})(y_{\mathrm{EMR}}-1.2x_{\mathrm{EMR}}^3 \\
& +3x_{\mathrm{EMR}}^2+k_1({a_1}^2+b_1\sin\varphi)x+I_1) \\
& +(2y_{\mathrm{EMR}}-2b_1\varphi)(1-5x_{\mathrm{EMR}}^2-y_{\mathrm{EMR}}) \\
& -(2b_1y_{\mathrm{EMR}}-2b_1^2\varphi)x_{\mathrm{EMR}}. \qquad (16)
\end{aligned}
$$

In order to investigate the relationship between the effect of externally forced current on the electrical activity and energy, the fixed parameters $a_1 = 0.5$, $b_1 = 1$, $k_1 = 1$, and the energy of the model and its derivatives when the externally forced current I_1 is 0.52 and 1, respectively, are investigated in Fig. 9. Where the red curve represents the action potential of the system, the blue curve represents the Hamiltonian energy of the system, and the green curve represents the rate of change of the energy. For the externally forced current I_1, as it increases, the energy also increases at this time, indicating that the externally forced current I_1 provides energy to the system. Action potentials, Hamiltonian energy, and the derivative of energy correspond to each other, indicating that energy is required to produce action potentials.

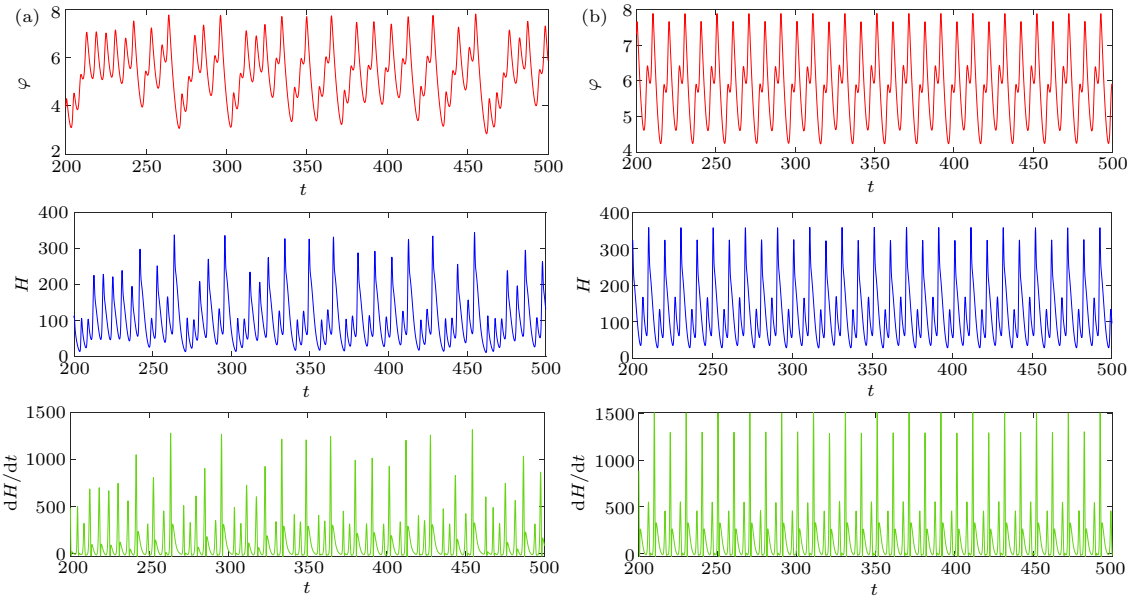


Fig. 9. Hamiltonian energy analysis: (a) externally forced current $I_1 = 0.52$; (b) externally forced current $I_1 = 1$.

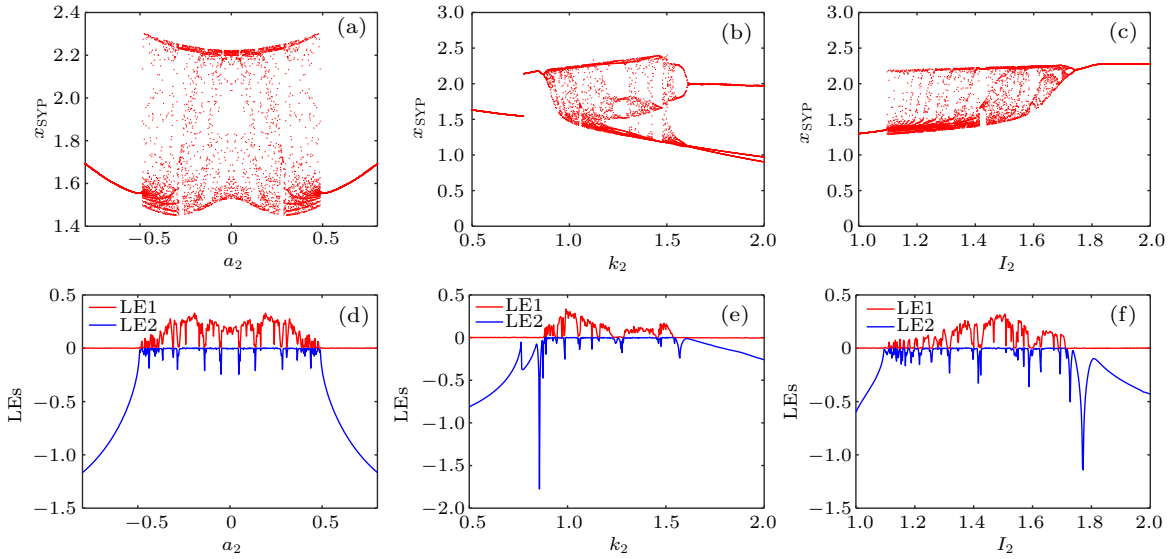


Fig. 10. The bifurcation diagrams and Lyapunov exponential spectra of different parameters regulation in scenario II: (a), (d) LAM's parameter a_2; (b), (e) coupling strength parameter k_2 of the LAM; (c), (f) external forcing current I_2.

For scenario II, parameter a enters the chaotic state by tangential bifurcation at $a_2 = -0.5$ and then returns to the periodic state again at $a_2 = 0.5$. For parameter k_2, the system first enters the chaotic state via a period-doubling bifurcation and then returns to the periodic state via an inverse period-doubling bifurcation. Parameter I_2 into the chaotic status abruptly via the tangent bifurcation, and finally into the periodic status via inverse period-doubling bifurcation. The relevant dynamical behavior is inscribed in Fig. 10.

Similarly, different external forcing currents result in dif-

ferent firing patterns in scenario II, as shown in Fig. 11. Each subplot in Fig. 11 shows the timing diagram of the external current at the top and the corresponding attractor phase diagram at the bottom. At external currents $I_2 = 1.1$, 1.3, and 1.4, scenario II exhibits bursting firing patterns, and at $I_2 = 1.65$, 1.73, and 1.8, scenario II exhibits spiking firing patterns.

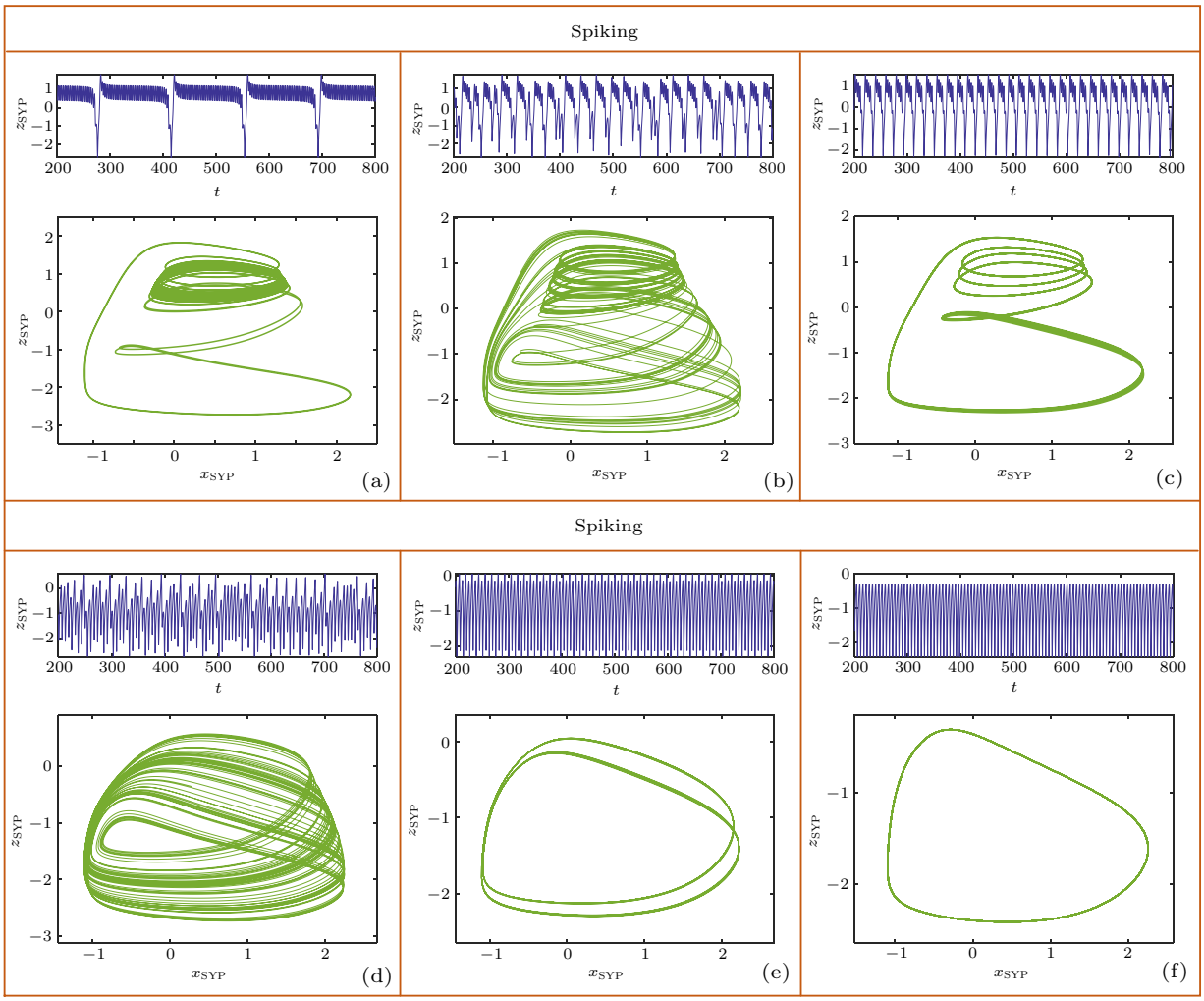


Fig. 11. Different firing patterns produced by applying different externally forced currents I_2 in scenario II: (a) bursting, $I_2 = 1.1$; (b) bursting, $I_2 = 1.3$; (c) bursting, $I_2 = 1.4$; (d) spiking, $I_2 = 1.65$; (e) spiking, $I_2 = 1.73$; (f) spiking, $I_2 = 1.8$.

4.2. Multistable behavior

The neuron model in scenario I has a multistable behavior under different initial conditions due to the introduction of the sinusoidal function. The fixed parameters $a_1 = 0.5$, $b_1 = 1$, $k_1 = 1$, and the initial conditions are (0, 0, $n\pi$), where $n = 0$, ± 2, and ± 4. For the externally forced current parameter, two typical values were chosen for analysis.

When $I_1 = 1.5$ is chosen, the model can generate an infinite number of homogeneous periodic coexisting attractors, and in this paper only five coexisting attractors are plotted in Fig. 12(a) as an example. The corresponding time-domain waveform plots and the attractor basin under this parameter are also inscribed as shown in Figs. 12(b) and 12(c). The attractor basin corresponds to the color of the attractor phase diagram and the time-domain waveform. When $I_1 = 0.62$ is chosen, the model produces infinitely many homogeneous chaotic coexisting attractors, as shown in Fig. 12(d), and similarly the time-domain waveform maps and the attractor basin for this condition are plotted as shown in Figs. 12(e) and 12(f). In Figs. 12(b) and 12(e), The time domain waveforms show that the chaotic signal can be controlled losslessly by changing the initial value of the memristor and the polarity of the signal can be switched freely, which is very important for the application in practical engineering. For the attractor basins in Figs. 12(c) and 12(d), different colors represent different attractor domains, and the boundaries of different attractor domains show a jagged shape, which indicates that the attractor basin boundary situation is very complicated. In fact, by changing different initial conditions, an infinite number of hidden attractors with the same shape but different positions can be obtained, thus exhibiting hidden homogeneous extreme multistability.

For scenario II, the initial value selected as (0, 0, 0) and (0, −10, 0), respectively, and when the parameters are chosen as $a_2 = 0.2$, $b_2 = -1$, $k_2 = 1.5$, and $I_2 = 1.2$, the attractor basins and the attractor phase trajectories are inscribed as

shown in Figs. 13(a) and 13(b). It can be seen that under this condition, the chaotic attractors converge to different attractor domains and they are entangled with each other. When the parameters are chosen as $a_2 = 0.2$, $b_2 = -1$, $k_2 = 0.7$, and $I_2 = 1.5$, then the attractor basin and periodic coexisting attractor as illustrated in Figs. 13(c) and 13(d).

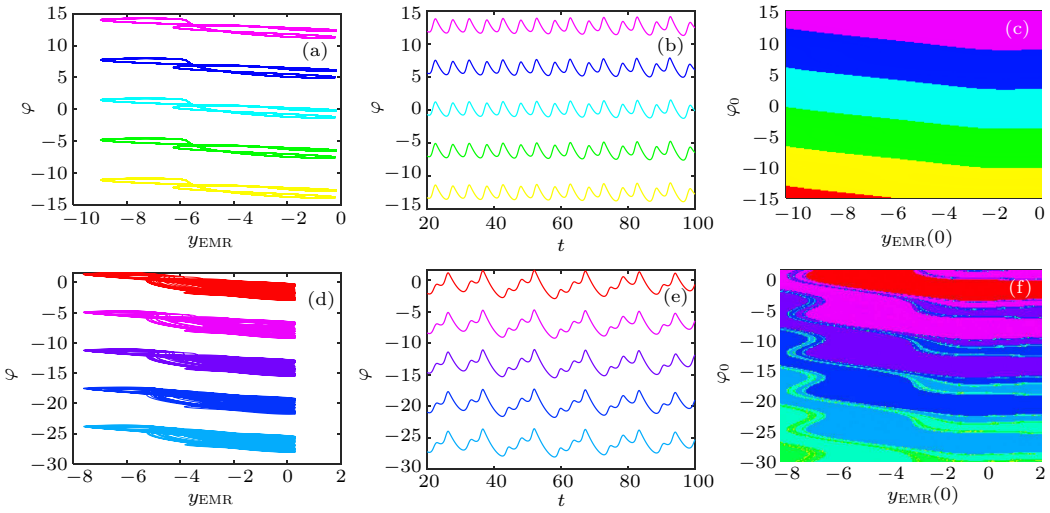


Fig. 12. Extreme multistability with hidden homogeneous exhibited under scenario I: (a)–(c) homogeneous periodic attractors' phase diagrams and their corresponding time-domain waveforms and attractor basins; (d)–(f) homogeneous chaotic attractors' phase diagrams and their time-domain waveforms and attractor basins.

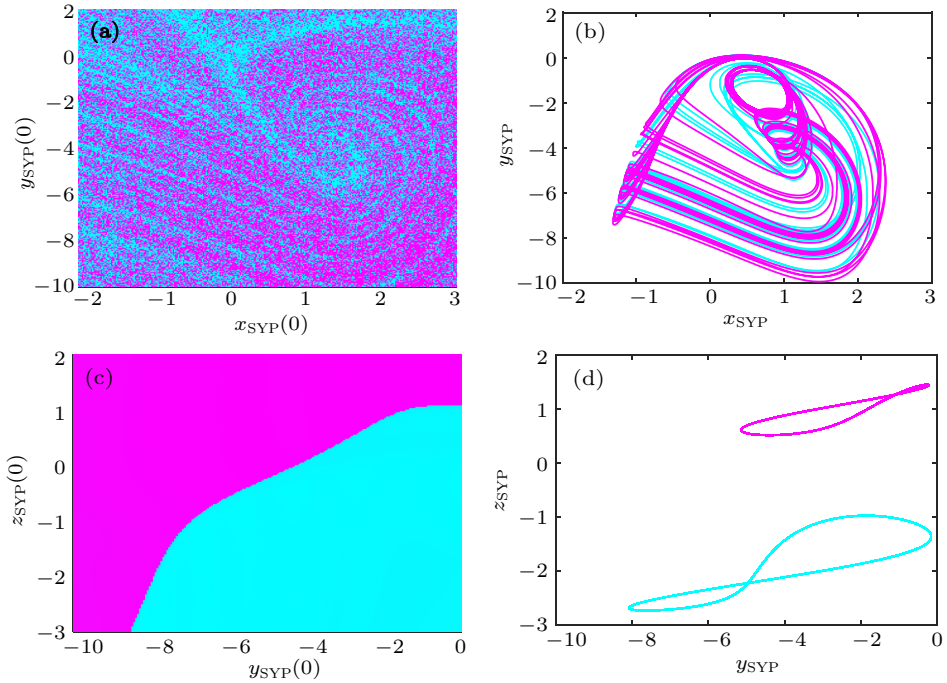


Fig. 13. Scenario II exhibits multistability: (a), (b) chaotic attractor basin and phase diagrams of chaotic attractor in it; (c), (d) periodic attractor basin and its corresponding periodic attractor phase trajectories.

4.3. Transient dynamical behavior

Transient dynamical behavior is a unique nonlinear phenomenon that occurs before a system evolves from one state of motion to a steady-state mode of motion, a process often accompanied by boundary crises. When the evolution of system dynamical behavior is explored on a time scale, the system exhibits a chaotic state for a finite time interval and then migrates to a stable nonchaotic state, a phenomenon known as transient chaos. Interestingly, for scenario I it is found that the system exhibits chaotic behavior at first, it then enters a periodic state, and finally enters again into a stable chaotic state. Setting the parameters $a_1 = 0.517$, $b_1 = 1$, $k_1 = 1.2$, $I_1 = 1$, and the initial condition (0, 0, π), the system exhibits a state dynamical behavior from chaos to period and back again in the time interval as shown in Fig. 14. For scenario II, with parameters $a_2 = 0.286$, $b_2 = -1$, $k_2 = 1$, $I_2 = 1.5$, and initial conditions (0, 0, π), the system exhibits transient chaotic behavior as shown in Fig. 15. In the figure, the dynamical behaviors corresponding to different states are indicated by different colors.

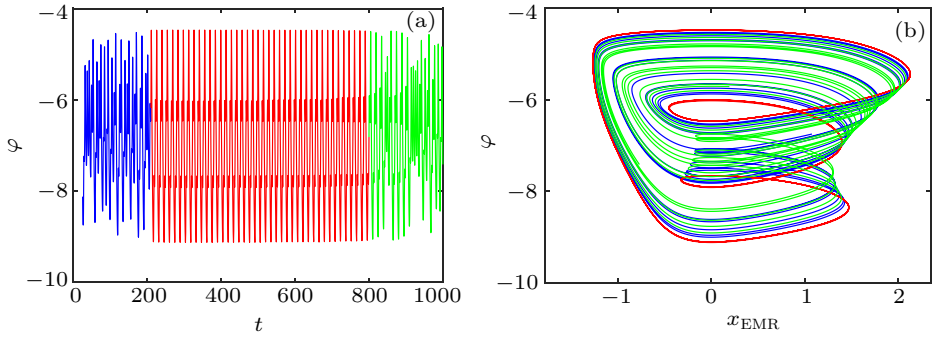


Fig. 14. Transient dynamical analysis in scenario I: (a) time domain waveform; (b) phase trajectories of attractors.

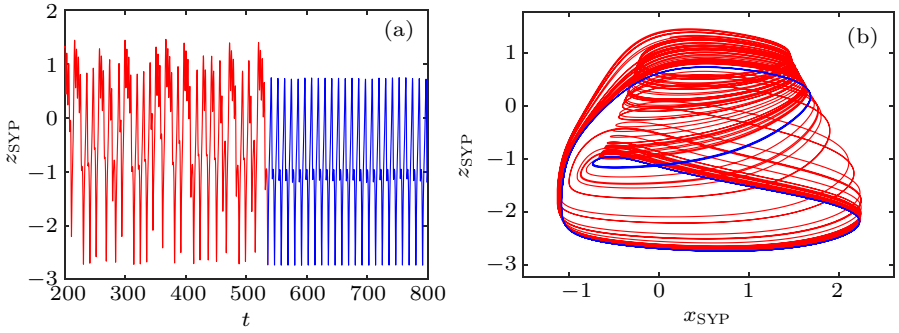


Fig. 15. Transient chaos in scenario II: (a) time domain waveform; (b) phase trajectories of attractors.

5. Complexity analysis in different scenarios

Through the previous analysis, the dynamical behavior of the system becomes complicated by the fact that the memristor acts as a synapse in the HR neuron model or the neuron model is stimulated by external electromagnetic stimulation. Chaotic sequences whose chaotic degree is closely related to the complexity. In general, the higher the degree of chaos, the higher the complexity. For nonlinear systems, examining their complexity is the key to dynamical analysis. Spectral entropy (SE) complexity describes the structural complexity of the sequence, which utilizes the Fourier transform to obtain the energy distribution in the transform domain, and then combines with the Shannon entropy to obtain the SE value. The more balanced the energy distribution is, the more complex is its spectral structure, and the closer the signal is to random oscillation, and the higher its complexity is. In this paper, the SE complexity algorithm is chosen to compute the two-parameter complexity spectrum of the studied parameters in different scenarios separately, as shown in Fig. 16. To ensure the accuracy of the experiments, the selected parameters and initial conditions were consistent with the dynamical analysis

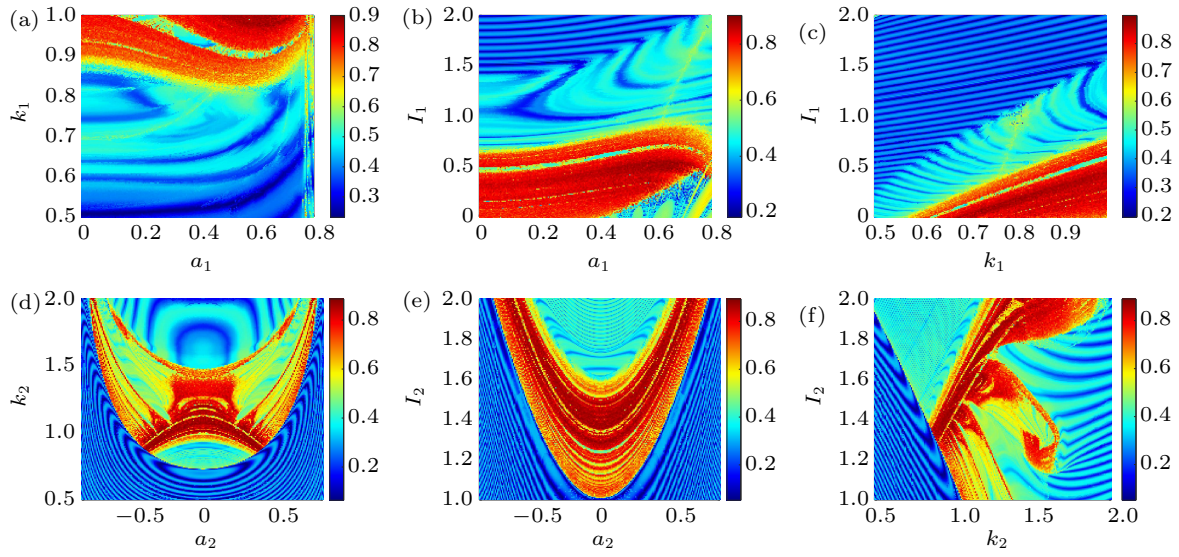


Fig. 16. Complexity maps for different scenarios: (a)–(c) complexity maps for typical parameters in scenario I; (d)–(f) complexity maps for corresponding parameters in scenario II.

described above. The change of color in the figure represents the change of high and low complexity. It can be seen that with the change of parameters, both scenario I and scenario II exhibit stable high and low complexity regions. It should also be noted that the complexity spectrum shown in Fig. 16 behaves consistently with the Lyapunov exponential spectrum and bifurcation diagrams of Figs. 7 and 10. When the parameter variations in different scenarios are in the periodic status, they have relatively low complexity, favoring blue in the complexity spectrum, and when they are in the chaotic state, they have relatively high complexity, favoring red color in the complexity spectrum. This further illustrates the controllability of chaotic sequences and the flexibility of parameter selection in practical engineering applications.

6. Hardware implementation

6.1. Circuit simulation

The construction of electronic neurons through analog circuits is essential for studying neuronal biological properties and designing neuronal integrated circuits. To validate firing patterns for the neural model in different scenarios, a manipulable analog circuit was designed using operational amplifiers, multipliers, resistors, and capacitors, as shown in Fig. 17. The main circuit of the neuron model is shown in the blue dashed box in the figure, and the memristor analog circuits in different scenarios are shown in the purple dashed box.

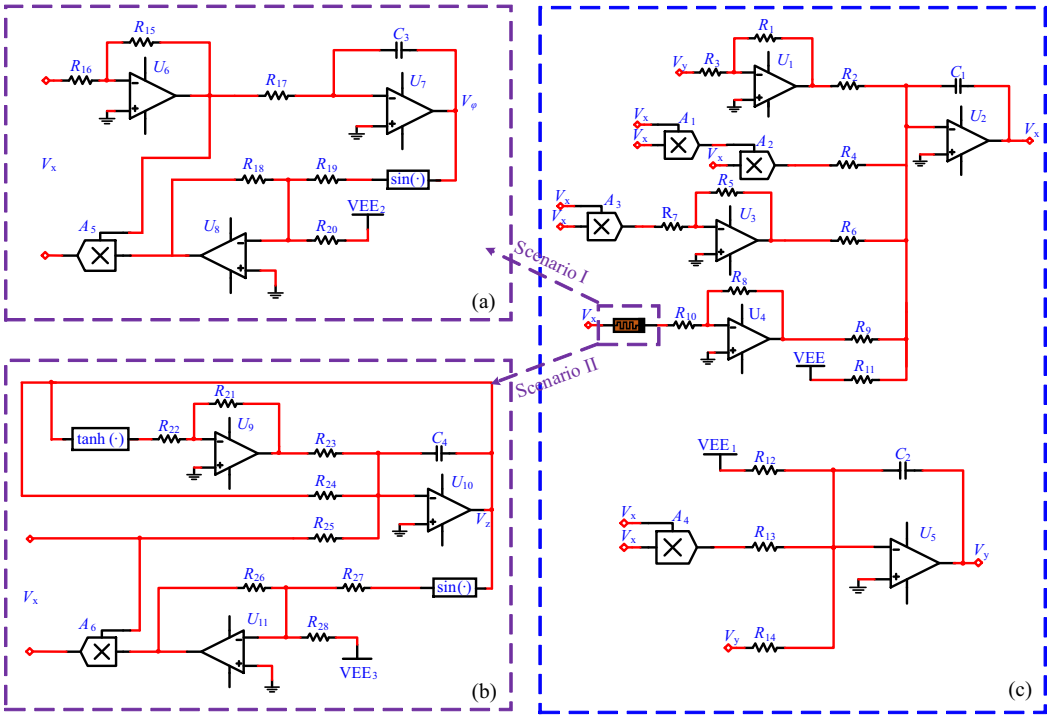


Fig. 17. The schematics of the neuron circuits: (a) analog circuit of the ideal memristor in scenario I; (b) analog circuit of the LAM in scenario II; (c) main circuit of the neuron model.

According to Kirchhoff's law, in scenario I the circuit equation of the neuron model is

$$\begin{cases} C_1\dfrac{\mathrm{d}V_x}{\mathrm{d}t} = \dfrac{R_1}{R_2R_3}V_y - \dfrac{1}{100R_4}{V_x}^3 + \dfrac{R_5}{10R_6R_7}{V_x}^2, \\ \qquad\qquad + \dfrac{R_8}{R_9R_{10}}\left(\dfrac{R_{18}}{R_{20}}\mathrm{VEE}_2 + \dfrac{R_{18}}{R_{19}}\sin(V_\varphi)\right)V_x \\ \qquad\qquad + \dfrac{1}{R_{11}}\mathrm{VEE}, \\ C_2\dfrac{\mathrm{d}V_y}{\mathrm{d}t} = \dfrac{1}{R_{12}}\mathrm{VEE}_1 - \dfrac{1}{10R_{13}}{V_x}^2 - \dfrac{1}{R_{14}}V_y, \\ C_3\dfrac{\mathrm{d}V_\varphi}{\mathrm{d}t} = \dfrac{R_{15}}{R_{16}R_{17}}V_x. \end{cases} \tag{17}$$

The corresponding circuit equation in scenario II is

$$\begin{cases} C_1\dfrac{\mathrm{d}V_x}{\mathrm{d}t} = \dfrac{R_1}{R_2R_3}V_y - \dfrac{1}{100R_4}{V_x}^3 + \dfrac{R_5}{10R_6R_7}{V_x}^2 \\ \qquad\qquad + \dfrac{R_8}{R_9R_{10}}\left(\dfrac{R_{26}}{R_{28}}\mathrm{VEE}_3 + \dfrac{R_{26}}{R_{27}}\sin(V_z)\right)V_x \\ \qquad\qquad + \dfrac{1}{R_{11}}\mathrm{VEE}, \\ C_2\dfrac{\mathrm{d}V_y}{\mathrm{d}t} = \dfrac{1}{R_{12}}\mathrm{VEE}_1 - \dfrac{1}{10R_{13}}{V_x}^2 - \dfrac{1}{R_{14}}V_y, \\ C_4\dfrac{\mathrm{d}V_z}{\mathrm{d}t} = \dfrac{R_{21}}{R_{23}R_{22}}\tanh(V_z) - \dfrac{1}{R_{24}}V_z - \dfrac{1}{R_{25}}V_x. \end{cases} \tag{18}$$

The V_x, V_y, V_φ and V_z in the two equations are the circuit state variables and VEE, VEE_1, VEE_2, and VEE_3 are the external bias voltages, respectively. The parameter values of each component in the circuit schematic are detailed in Ta-

ble 2. By adjusting the resistance values of resistor R_9 in the circuit of scenario I to 188.679 kΩ, 153.846 kΩ, 129.870 kΩ, and 117.647 kΩ, which corresponds to the coupling strength parameter k_1 of 0.53, 0.65, 0.77, and 0.85, the firing results of the analog circuit are obtained as shown in Fig. 18. Adjusting the resistance values of the resistor R_{11} of the circuit in scenario II to 90.909 kΩ, 76.923 kΩ, 71.428 kΩ, 60.606 kΩ, 57.803 kΩ, and 55.556 kΩ, corresponding to the external forcing current parameter I_2 of 1.1, 1.3, 1.4, 1.65, 1.73, and 1.8, respectively, obtains the different firing results as shown in Fig. 19. Note that the VEE is set to 0.6 V in scenario I and 1.5 V in scenario II. The experimental results show that the firing behavior can be captured in the different scenarios, which further demonstrates the validity of the numerical simulation.

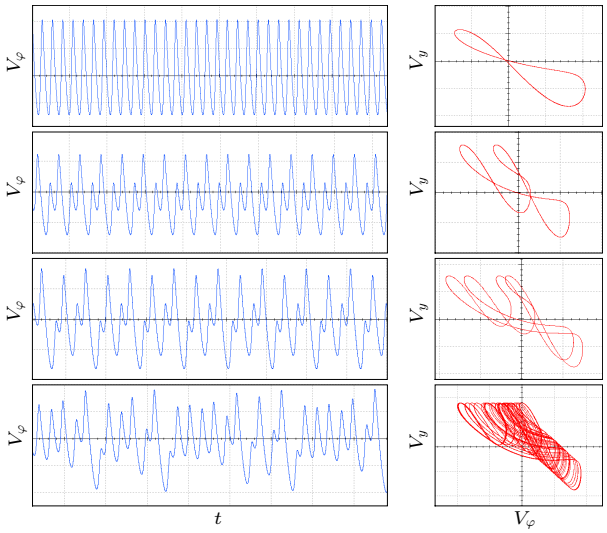


Fig. 18. The results of firing experiment in scenario I.

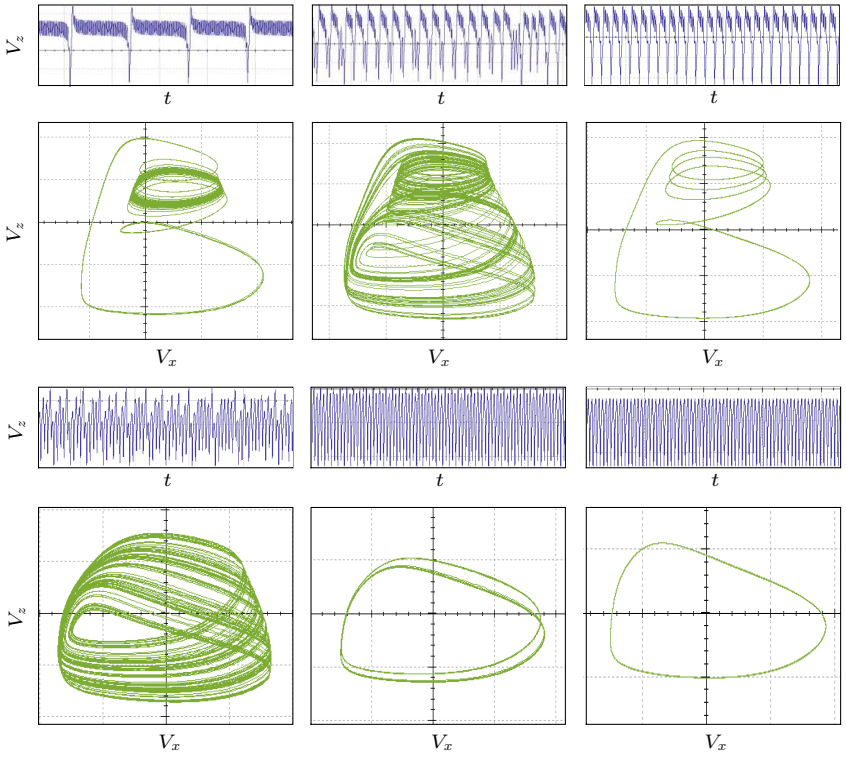


Fig. 19. Firing results captured experimentally in scenario II.

Table 2. Parameters of each component in the circuit diagram.

Parameters	Elements	Values
$R_1, R_3, R_5, R_7, R_8, R_{10}, R_{15}, R_{16}, R_{18}, R_{19}, R_{20}, R_{21}, R_{22}, R_{26}, R_{27}, R_{28}$	resistance	10 kΩ
$R_2, R_9, R_{11}, R_{12}, R_{14}, R_{17}, R_{24}, R_{25}$	resistance	100 kΩ
R_4	resistance	83.3 kΩ
R_6	resistance	33.3 kΩ
R_{13}	resistance	20 kΩ
R_{23}	resistance	50 kΩ
R_9	resistance	adjustable
R_{11}	resistance	adjustable
C_1, C_2, C_3, C_4	capacitance	10 nF
$A_1, A_2, A_3, A_4, A_5, A_6$	multiplier	0.1
VEE	voltage	0.6 V (1.5 V)
VEE_1	voltage	1.0 V
VEE_2	voltage	0.25 V
VEE_3	voltage	0.04 V

6.2. DSP implementation

For chaotic systems, the ability to realize them in hardware is a prerequisite for practical engineering applications. DSP is widely used in industrial electronics due to its excellent performance of low cost and power consumption, and high stability. Therefore, in this section, the hardware realization of scenario I and scenario II by developing DSP is shown in Fig. 20. Figure 20(a) shows the real-time status of the system hardware implementation. The hardware implementation platform includes a DSP microprocessor (TMS320F28335), a D/A converter (DAC8552) and an XDS emulator as illustrated in Fig. 20(b). Figure 20(c) shows the chaotic attractor captured by oscilloscope in the φ–y phase plane for scenario I, and Figs. 20(d) and 20(e) show the attractor phase trajectories in the x–y plane and x–z plane for scenario II, respectively. It can be seen that the attractor trajectories captured by the oscilloscope are consistent with the Matlab simulation results, which fully illustrates the validity of the proposed model.

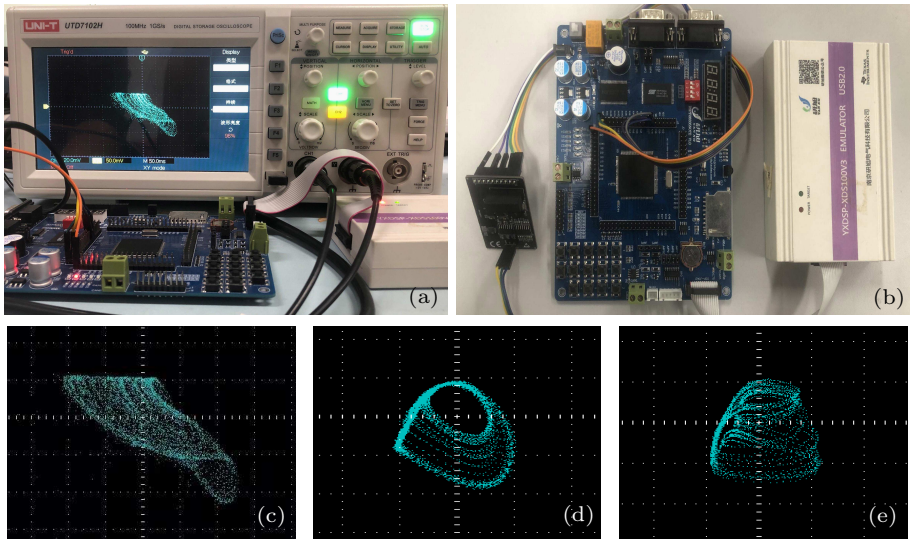


Fig. 20. Experimental platform and attractor trajectories captured by the oscilloscope in different scenarios: (a) real-time state of the hardware; (b) realization platform; (c) φ–y phase plane, scenario I; (d) x–y phase plane, scenario II; (e) x–z phase plane, scenario II.

7. Conclusion

An ideal flux memristor with sinusoidal mode conductance is utilized to describe the electromagnetic induction effect of biological neurons in this work. Meanwhile, a novel LAM based on the ideal memristor is proposed to replace the biological neuron synapses. The effects on the existing 2D HR neuron model in these two scenarios are described. In the subsequent study, it is shown that the constructed biological neuron model has multiple firing modes. The relationship between firing patterns and energy was revealed by Hamiltonian energy analysis. The neuronal models showed multistable excitation phenomena in both electromagnetic stimulation and the LAM simulation of synapses. Studying the complex multistable behavior of biological neuronal models helps to understand behavioral mechanisms such as brain memory. Subsequently, the neuronal models in different scenarios are evaluated using the SE complexity algorithm, and the results obtained show that the introduction of the memristors makes the neuronal models in both scenarios highly complex, which further proves the appropriateness of choosing different memristors to simulate different scenarios. The state transition and transient chaos phenomena of different scenarios are also explored. Finally, the numerical simulation results are verified by circuit simulation and DSP hardware implementation. This provides the possibility of practical engineering applications for the memristor-based biological neural model.

Acknowledgements

Project supported by the National Natural Science Foundation of China (Grant No. 62061014), Technological Innovation Projects in the Field of Artificial Intelligence in Liaoning province (Grant No. 2023JH26/10300011), and Basic Scientific Research Projects in Department of Education of Liaoning Province (Grant No. JYTZD2023021).

References

[1] Yao Z, Zhou P, Zhu Z and Ma J 2021 *Neurocomputing* **423** 518
[2] Lv M, Wang C, Ren G, Ma J and Song X 2016 *Nonlinear Dyn.* **85** 1479
[3] Han Z, Sun B, Banerjee S and Mou J 2024 *Chaos Soliton. Fract.* **184** 115020
[4] Ma T, Mou J, Banerjee S and Cao Y 2023 *Chaos Soliton. Fract.* **174** 114113
[5] Wang X, Du J, Li Z, Ma M and Li Z 2024 *Acta Phys. Sin.* **73** 110503 (in Chinese)
[6] Hodgkin A L and Huxley A F 1952 *The Journal of Physiology* **117** 500
[7] Hindmarsh J L and Rose R 1982 *Nature* **296** 162
[8] Fitzhugh R 1960 *The Journal of General Physiology* **43** 867
[9] Nagumo J, Arimoto S and Yoshizawa S 1962 *Proceedings of the IRE* **50** 2061
[10] Izhikevich E M 2003 *IEEE Transactions on Neural Networks* **14** 1569
[11] Dahasert N, Öztürk İ and Kiliç R 2012 *Nonlinear Dyn.* **70** 2343

[12] Zhang S, Zheng J, Wang X and Zeng Z 2021 *Chaos Soliton. Fract.* **145** 110761
[13] Korkmaz N, Öztürk İ and Kiliç R 2016 *Nonlinear Dyn.* **86** 1841
[14] Li C, Wang X, Du J and Li Z 2023 *Nonlinear Dyn.* **111** 21333
[15] Lv M and Ma J 2016 *Neurocomputing* **205** 375
[16] Wu F, Gu H and Li Y 2019 *Communications in Nonlinear Science and Numerical Simulation* **79** 104924
[17] Zhao Z, Li L, Gu H and Gao Y 2020 *Nonlinear Dyn.* **99** 1129
[18] Ma H, Jia B, Li Y and Gu H 2021 *Neural Plasticity* **2021** 6692411
[19] Xie Y, Yao Z and Ma J 2023 *Science China Technological Sciences* **66** 439
[20] Chua L 1971 *IEEE Transactions on Circuit Theory* **18** 507
[21] Mou J, Ma T, Banerjee S and Zhang Y 2024 *IEEE Transactions on Circuits and Systems I: Regular Papers* **71** 1771
[22] Li R and Ding R 2021 *International Journal of Modern Physics B* **35** 2150166
[23] An X and Qiao S 2021 *Chaos Soliton. Fract.* **143** 110587
[24] Lu L, Jia Y, Liu W and Yang L 2017 *Complexity* **2017** 7628537
[25] Bao H, Zhu D, Liu W, Xu Q, Chen M and Bao B 2020 *International Journal of Bifurcation and Chaos* **30** 2050045
[26] Li K, Bao H, Li H, Ma J, Hua Z and Bao B 2021 *IEEE Transactions on Industrial Informatics* **18** 1726
[27] Bao H, Hu A, Liu W and Bao B 2019 *IEEE Transactions on Neural Networks and Learning Systems* **31** 502
[28] Chua L O 2005 *International Journal of Bifurcation and Chaos* **15** 3435
[29] Liu X, Mou J, Zhang Y and Cao Y 2023 *IEEE Transactions on Industrial Electronics* **71** 5094
[30] Han Z, Al-Barakati A, Hadi J and Mou J 2024 *Nonlinear Dyn.* **112** 4863
[31] Ma Y, Mou J, Banerjee S and Miao M 2023 *Applied and Computational Mathematics* **22** 317
[32] Ying J, Liang Y, Wang J, Dong Y, Wang G and Gu M 2021 *Chaos Soliton. Fract.* **148** 111038
[33] Mou J, Han Z, Cao Y and Banerjee S 2024 *IEEE Transactions on Circuits and Systems–II: Express Briefs* **71** 2824
[34] Ma Y, Mou J, Jahanshahi H, Alkhateeb A F and Bi X 2023 *Chaos Soliton. Fract.* **173** 113708
[35] Wang L, Zhou N, Sun B, Cao Y and Mou J 2024 *Chin. Phys. B* **33** 050501
[36] Zhang Z, Mou J, Banerjee S and Cao Y 2024 *Chin. Phys. B* **33** 020503
[37] Xie W, Wang C and Lin H 2021 *Nonlinear Dyn.* **104** 4523
[38] Wang X, Cao Y, Li H and Li B 2023 *Fractal and Fractional* **7** 582
[39] Chen X, Banerjee S, Cao Y and Mou J 2023 *International Journal of Bifurcation and Chaos* **33** 2350190
[40] Sha Y, Mou J, Banerjee S and Zhang Y 2023 *IEEE Transactions on Industrial Informatics* **20** 3835
[41] Jin P, Wang G, Liang Y, Iu H H C and Chua L O 2021 *IEEE Transactions on Circuits and Systems I: Regular Papers* **68** 4419
[42] Gao X, Sun B, Cao Y, Banerjee S and Mou J 2023 *Chin. Phys. B* **32** 030501
[43] Lai Q and Yang L 2023 *Chaos Soliton. Fract.* **174** 113807
[44] Ma X, Li C, Li Y, Bi L and Qi Z 2022 *Euro. Phys. J. Plus* **137** 542
[45] Li R, Wang Z and Dong E 2021 *Nonlinear Dyn.* **104** 4459
[46] Breakspear M 2017 *Nature Neuroscience* **20** 340
[47] Ren L, Qin L, Hadi J and Mou J 2023 *International Journal of Bifurcation and Chaos* **33** 2350197
[48] Doubla I, Njitacke Z, Ekonde S, Tsafack N, Nkapkop J and Kengne J 2021 *Neural Computing and Applications* **33** 14945
[49] Cao H, Wang Y, Banerjee S, Cao Y and Mou J 2024 *Chaos Soliton. Fract.* **179** 114466
[50] Liu B, Peng X and Li C 2024 *International Journal of Electronics and Communications* **178** 155283
[51] Hu X, Wang S and Liu C 2022 *Chinese Journal of Physics* **77** 2541
[52] Santana L, da Silva R M, Albuquerque H and Manchein C 2021 *Chaos* **31** 053107